PNAS
www.pnas.org

Supporting Information for

Ionization behavior of nanoporous polyamide membranes

Cody L. Ritt[1], Jay R. Werber[1], Mengyi Wang[2,3], Zhongyue Yang[2], Yumeng Zhao[1], Heather J. Kulik[2], and Menachem Elimelech[1*]

[1] Department of Chemical and Environmental Engineering, Yale University, New Haven, Connecticut 06520-8286

[2] Department of Chemical Engineering, Massachusetts Institute of Technology, Cambridge, Massachusetts 02139

[3] Department of Materials Science and Engineering, Massachusetts Institute of Technology, Cambridge, Massachusetts 02139

Contents:

26 Pages

15 Figures

8 Tables

*Corresponding author: Menachem Elimelech, Email: menachem.elimelech@yale.edu, Phone: (203) 432-2789

www.pnas.org/cgi/doi/10.1073/pnas.2008421117

Estimation of Pore Size via the Hindered Transport Model

The average pore size of the NF270 and LIP membranes was estimated by hindered transport model (HTM), which accounts for steric exclusion as well as hindered convection and diffusion of neutral organic solutes (1). The values obtained from HTM should not be considered absolute, as the highly cross-linked network structure of polyamide films can lead to deviations in the predictions of HTM (2). Nonetheless, results from HTM can be used for relative comparison of the porous environment.

We employed dextrose (≥99%, Sigma-Aldrich, St. Louis, MO) as a neutrally charged, low molecular weight organic tracer (Fig. S4*A*) (3). Prior to testing, the membranes were compacted in DI water under 12.1 bar (175 psi) of hydraulic pressure overnight. After compaction, 50 mg L^{-1} as total organic carbon (TOC) of the organic solute was circulated in the membrane system. Permeate samples were collected at 6.20, 7.58, 8.96, and 10.34 bar (90, 110, 130, and 150 psi) applied pressure for LIP membranes and 1.38, 4.14, 6.89, and 9.65 bar (20, 60, 100, and 140 psi) for NF270 with a crossflow velocity of 21.4 cm s^{-1} and feed solution temperature of 25.0 ± 0.5 °C. The permeate samples were taken after the system was allowed to equilibrate for 30 min at each pressure. Solute concentration was determined by analyzing permeate and feed samples for TOC (TOC V-CSH, Shimadzu Corp., Kyoto, Japan).

The real rejection of the organic solutes (R_r) is determined by

$$R_r = 1 - \frac{\Phi K_c}{1 - \exp(-Pe)(1 - \Phi K_c)} \tag{S1}$$

where Φ is the partition coefficient of the solute, K_c is the hydrodynamic hindrance coefficient, and *Pe* is the Peclet number. We used film thicknesses from AFM measurements of each membrane (Fig. 1*C* of main text) and assumed a porosity of 0.04. Details on the calculation of K_c and *Pe* are given elsewhere (1). The partition coefficient assumes only steric interactions in a cylindrical pore (4):

$$\Phi = \frac{\langle c' \rangle}{c} = \left(1 - \frac{r_s}{r_p}\right)^2 \tag{S2}$$

where c and $\langle c' \rangle$ are the concentration just outside the pore and average concentration just inside the pore, respectively. The ratio of these values is related to the ratio of solute radius (r_s) to the pore radius (r_p).

Equation (S1) can be used to determine the solute concentration at the membrane surface with concentration polarization effects considered. To relate the observed rejection (R_o) to R_r, we apply film theory (1, 3):

$$\ln \frac{1 - R_r}{R_r} = \ln \frac{1 - R_o}{R_o} - \frac{J_W}{k_f} \tag{S3}$$

where k_f is the feed mass transfer coefficient and J_W is the water flux across the membrane. The membrane pore size was finally estimated from the solute rejection data after performing an optimization process reported elsewhere (Fig. S4*B*) (1).

Anomalous Zeta Potential Signal at High pH

In principle, the streaming potential generated from flowing an electrolyte solution across a stationary surface should only be influenced by fixed charged groups located at the surface (5). Therefore, the zeta potential should be a product of only ionized carboxyl ($R\text{-}COO^-$) and amine ($R_2\text{-}NH_2^+$) groups at the surface, and hence, should only exhibit a single pK_a around pH 5 (based on findings in the manuscript). However, the appearance of a second pK_a located around pH 9 resembles the trends observed in our silver-binding assay (Main text Fig. 2b), suggesting that streaming potential may be generated from within the membrane film. This unexpected finding raises the question: are potential measurements isolated to the surface of NF membranes?

This is the first time, to our knowledge, that a second pK_a has been observed in zeta potential analysis of NF membranes. The novelty of this phenomenon is likely the consequence of previously published works only assessing membrane zeta potentials up to pH 9 (5-7), where the inflection point would just begin. In fact, high resolution zeta potential analysis of several polyamide-based NF membranes depicts the inception of an inflection point at pH 9 (7), mirroring data presented in Fig. 2f of the main text. The extent to which the flowing electrolyte solution that is used to generate streaming potential could penetrate the film is unclear, but such a circumstance is plausible as NF membranes often display low KCl rejection (8).

We compared NF270 and SW30XLE to investigate the role of electrolyte penetration in zeta potential analysis (Fig. S5). SW30XLE, a widely used seawater reverse osmosis (SWRO) membrane, is capable of achieving NaCl rejection greater than 99.5% for feed salinities ~0.6 M and thus should have limited penetration by the streaming electrolyte solution (9, 10). Furthermore, SW30XLE was also reported to ionize similarly to NF270 (11), displaying two pK_a values for R-COOH ionization. Despite similarities in R-COOH ionization, a second pK_a did not materialize for SW30XLE during zeta potential analysis. The absence of p$K_{a,2}$ in SW30XLE during streaming potential measurements likely stems from the inability of KCl to penetrate the dense, non-porous RO film. This corroborates our belief that the development of a second pK_a during zeta potential analysis for LIP and NF270 membranes is the result of penetration by the electrolyte solution into the semi-porous NF films.

Our findings suggest that zeta potential analysis of NF membranes partially detect interior charged groups, in addition to the expected surface groups. However, we note that the contribution to streaming potential from charged groups within the film is minor. The cumulative potential drop from the ionization of R-COOH on the surface of the LIP membranes (7.0–9.5 mV) is similar to the cumulative potential drop from the ionization of interior R-COOH (6.7–7.9 mV). With a roughly tenfold difference in the volumetric densities of surface and interior R-COOH (Main text Fig. 2c), we would expect a substantially larger disparity between the potential drops associated with p$K_{a,1}$ and p$K_{a,2}$ if all interior $R\text{-}COO^-$ were influencing streaming potential measurements.

Electrostatic Exclusion Mechanisms

Our experimental results provide some insight into the mechanism of ion exclusion within the film. It has been suggested in recent models that electrostatic exclusion of salt by interior R-COO$^-$ is largely dielectric in nature, rather than from the formation of a Donnan potential across the membrane (12, 13). Although the interpretation of dielectric exclusion varies, both can be physically conceived by examining the scale of the Bjerrum length (λ_B), which governs Coulombic interactions (14), relative to the separation between fixed charges. The Bjerrum length is defined as the distance between ions where the electrostatic interaction energy is equal in magnitude to thermal energy (k_BT) (12):

$$\lambda_B = \frac{e^2}{4\pi\varepsilon_r\varepsilon_0 k_B T} \tag{S4}$$

where e is elementary charge (1.60×10^{-19} C), ε_r is the relative permittivity, ε_0 is the permittivity of a vacuum (8.85×10^{-12} C^2 J^{-1} m^{-1}), k_B is the Boltzmann constant (1.38×10^{-23} J K^{-1}), and T is the absolute temperature (K). The Debye length approximates the extent of meaningful electrostatic influence from a charged surface exerting a potential when the thermal energy is large (12). Specifically, the Debye length quantitatively describes the thickness of the diffuse layer by (15)

$$\lambda_D = \frac{1}{\sqrt{8\pi\times10^3 N_A I \lambda_B}} \tag{S5}$$

where N_A is Avogadro's number (6.02×10^{23} mol^{-1}) and I is the ionic strength of solution (mol L^{-1}).

The exclusion of co-ions by fixed charged groups on membranes, referred to as Donnan exclusion, has often been explained by co-ion repulsion within the diffuse layer. However, the Debye length is inapplicable when its scale is commensurate, or even smaller, than the Bjerrum length (Fig. S15*A*). In a confined, low-dielectric environment, the Debye-Hückel theory—as well as the notion of Debye length—break down entirely. For charged membranes, the dielectric constant at which this breakdown occurs may be expressed as (12)

$$\varepsilon_r < \frac{e^2}{4\pi\varepsilon_0 k_B T} X^{1/3} \tag{S6}$$

where X is the volumetric charge density (mol L^{-1}). Taking a charge density of 0.5 mol L^{-1} for our membranes (Fig. 2*C* of the main text), we can estimate a Debye breakdown below a dielectric constant of ~45 (Fig. S15*B*).

Our results also have implications for ion association within the polyamide film. Assuming a local dielectric constant between 20 and 50 within the membrane pore, we can estimate a Bjerrum length of 1.12–2.80 nm. Given an average interior volumetric R-COOH density of 0.25 sites/nm^3 when fully ionized at high pH (Fig. 2*E* of main text), the average separation of fixed charges in the NF270 and LIP membranes can be estimated as ~1.6 nm using the relationship $b \approx X^{-1/3}$ (12).

The point at which λ_B and b are equivalent is considered the critical charge density, per the Manning Condensation model (16). When $\lambda_B > b$, some counter-ions may find themselves within the range of overlapping Bjerrum lengths from neighboring fixed charges. These counter-ions will be dominated by electrostatics as they lack sufficient thermal energy to diffuse away, leading to association, or "condensation," with the fixed charge (12, 14, 16). The oft-used Debye length is inapplicable under these conditions and should not be central to the discussion of charge-based exclusion in low-dielectric nanopores. Based on our estimates of λ_B and b above, the two are commensurate in the NF270 and LIP membranes studied here, suggesting that ion association may occur under some circumstances. However, the above analysis pertains to interior R-COOH at high pH. Given the heterogeneous ionization behavior in the polyamide film—as well as the presence of positive and negative charges at some pH levels—ion association behavior is likely more complicated.

Comparing Electrostatic and Non-Electrostatic Exclusion Mechanisms in Loose Polyamide

We compared the inverse salt permeance at pH 5, 7, and 10.5 (Fig. S10). Our analysis follows classic membrane transport models (17, 18), wherein the overall resistance experienced by a permeating species is the inverse of its permeance across the membrane. Salt resistance at pH 5, which is loosely considered the isoelectric point of polyamide membranes (19), is predominantly the result of solute exclusion from non-electrostatic effects like steric hindrance due to the lack of co-ion repulsion at this pH. For higher pH, changes in salt resistance can be attributed to electrostatic effects from functional group ionization.

We find an interplay between electrostatic and non-electrostatic exclusion mechanisms. As the thickness of the polyamide film increases from 1L to 5L PIP, resistances at pH 5 increase only slightly. Due to the absence of $R\text{-}COO^-$ at pH 5, the increase in salt resistance is likely non-electrostatic in nature and can be ascribed to the mode of operation as well as the diffusive transport of ions and water across the thicker membrane. Salt permeance is defined as the salt permeability over film thickness (i.e., $B = P_S/\delta$). Based on experimental evidence provided in the manuscript, we can assume that the LIP membranes share similar chemical structures. Related to our argument in the main text for comparable hydraulic water permeability, this should also result in comparable P_S. As such, the increase in salt resistance for thicker films at pH 5 (Fig. S10) is to be expected. The increase in salt resistance at pH 7, where surface R-COOH are expected to ionize, can be attributed to the slight increase in surface roughness from 1L to 5L PIP (Fig. 1*C* of the main text). We find a significant increase in the salt transport resistance for all the membranes at pH 10.5, which should be the result of interior R-COOH ionization. The largest change in resistance occurs between pH 7 and 10.5, which implies that the complete ionization of interior R-COOH at pH 10.5 imposes the greatest resistance to salt transport.

Layered Interfacial Polymerization (LIP)

Layered TFC NF membranes were fabricated by forming several sequential polyamide selective layers atop prewetted PS20 (Sepro) support membranes via LIP. The aqueous amine solution used for forming the polyamide layer consisted of 1.0 wt% PIP, 0.5 wt% triethylamine, and 0.15 wt% NaOH in deionized water. Wetted PS20 supports were immersed in the aqueous PIP-based amine solution for 90 s. Afterward, the PIP solution was poured off, and residual PIP solution was

removed from the membrane surface using a rubber plate roller (Sigma-Aldrich, St. Louis, MO). The PIP-soaked PS20 supports were then immediately immersed in 0.15 wt% TMC in hexane for 30 s, resulting in the formation of a thin polyamide film. For membranes requiring additional layers, the formed polyamide film was briefly rinsed with hexane and allowed to air dry for 120 s. After air drying, the polyamide film was re-immersed in the PIP solution and allowed to sit for 90 s before being poured off, with residual PIP removed once again with the rubber roller. Immediately after, the PIP-soaked polyamide films were immersed in the previously described TMC solution for 30 s, resulting in the formation of an additional polyamide layer. This process was repeated for the desired number of layers (Fig. 1*A* of the main text). After depositing the final polyamide layer, the TFC membranes were rinsed in hexane before being allowed to air dry for 120 s, thoroughly rinsed with deionized water, and finally stored in deionized water at 4 °C.

Preparation Methods for Film Characterization

To prepare microtome sections for transmission electron microscopy (TEM) characterization, the membranes were wetted, and the fabric backing was removed to reduce wrinkles in the microtome section. Afterward, wetted samples were cut into small wedges and embedded with a water-miscible acrylic resin (LR White) as reported previously (20). After curing at 65 °C for 24 hours, 50-nm thick cross-sections were prepared using a Leica Ultramicrotome UC7 (Leica Microsystems, Wetzlar, Germany) with a diamond knife (2.5 mm Ultra 45°, Diatome) and mounted onto formvar (stabilized with carbon) coated copper grids (Formvar/Carbon, Ted Pella, Redding, CA). Images were captured at 43,000× magnification.

For AFM, small sections of the polyamide films were isolated on a clean silicon wafer after physically removing the fabric backing and dissolving the PSf support layer. The polyamide film was then gently sliced in several locations with a metal precision glide needle (18G × 1 in., Becton Dickinson & Co., Franklin Lakes, NJ). Regions near the edge of the sliced sections were scanned using a Bruker Dimension FastScan AFM with a FastScan-B tip (5 nm tip radius, Bruker, Billerica, MA) in tapping mode at a scan rate of 3 Hz. The depth profiles were averaged over a 2 μm × 1 μm segment running perpendicular across the edge of the polyamide films (Fig. S1). Depth profiling was conducted in locations with minimal artifacts to avoid interference from bubbles, wrinkles, and any remaining PSf residue. The same method was applied with a Bruker Dektak XT stylus profilometer (Bruker, Billerica, MA) to determine film swelling by measuring the dry and swollen film thickness. This instrument was applied instead of an AFM to avoid corrosion of the aluminum AFM probe holder at high pH, allowing us to assess swelling over a wide pH range. The profilometer stylus has a z-resolution of ~5 nm and tip radius of 12.5 μm. The stylus force was set to 5 mg.

Quantification of Ionized Carboxyl and Amine Functionalities

Stock solutions of 40 µM silver nitrate ($AgNO_3$) and 1 µM $AgNO_3$ were prepared for the silver binding and surface washing steps, respectively. Bind- and wash-solutions were adjusted to their desired pH with NaOH and HNO_3. The backing-free membranes were submerged in the bind and wash solutions, repeated 2× and 4×, respectively. Membranes were subsequently blotted dry and immediately immersed in 5 mL of 1% HNO_3 (30 min) to elute bound silver. Silver-free membranes were removed from the acid solution and discarded. The same procedure was repeated when assessing amine ionization, but with 100 µM sodium bromide (NaBr) and 1 µM NaBr as bind- and

wash-solutions, respectively. Additionally, HBr was used for acidic pH adjustments. Bound bromide was eluted from the membranes with 10^{-3} M NaOH.

Eluted silver and bromide concentrations were converted to areal R-COO^- and R_2-NH_2^+ densities, respectively, by assuming 1:1 binding between Ag^+ and R-COO^- throughout the film (11, 21-23). This assumption was recently validated via FTIR spectroscopy in precisely controlled model polyamide films (24). Ion chromatography (930 Compact IC Flex with Metrosep A Supp 5- 150/4.0 column and conductivity detector, Metrohm, Herisau, Switzerland), was used to analyze eluted bromide, using a calibration curve ranging from 0 to 100 µg L^{-1}. Bromide concentration was similarly converted to areal R_2-NH_2^+ by assuming 1:1 binding between Br^- and R_2-NH_2^+ throughout the film. Therefore, the areal densities of R-COO^- and R_2-NH_2^+ (number of groups per nm^2), are as follows:

$$[\mathrm{R-COO^-}]_\mathrm{A} = C_{\mathrm{Ag^+}}\left(\frac{VN_\mathrm{A}}{A}\right) \tag{S7}$$

$$[\mathrm{R_2-NH_2^+}]_\mathrm{A} = C_{\mathrm{Br^-}}\left(\frac{VN_\mathrm{A}}{A}\right) \tag{S8}$$

where C_{Ag+} and C_{Br-} are the measured silver and bromide concentrations (M), respectively, V is the elution volume, N_A is Avogadro's number, and A is the projected surface area of the polyamide film (nm^2). The projected surface area of the membrane is defined as its single-sided surface area, neglecting surface roughness. We divided the areal R-COO^- density by the dry film thickness, measured by AFM, to obtain the volumetric R-COO^- density, $[\mathrm{R-COO^-}]_\mathrm{v} = [\mathrm{R-COO^-}]_\mathrm{A} / \delta_\mathrm{d}$ (number of groups per nm^3).

A carboxylate-based weak acid ion exchange (IEX) resin (Dowex MAC-3, DuPont, Wilmington, DE) was used to demonstrate the effect of ionic strength on carboxylate pK_a. Prior to use, the IEX resin was acidified in 1% HNO_3, washed with water to remove excess acid, and oven dried at 60 °C. Dried IEX resin (1 g) was mixed in 50 mL of deionized water. Titrations were conducted in deionized water, 10 mM $NaNO_3$, and 100 mM $NaNO_3$. After every addition of titrant, ample time (typically > 30 min) was allowed for the IEX resin to reach equilibrium with the solution and the pH of the supernatant was measured. The counter-ion uptake was calculated as V_tC_t/m, where V_t is the volume of titrant, C_t is the concentration of titrant, and m is the mass of dry resin used for titration.

Characterization of Nanofiltration Performance

The effective membrane surface area during filtration experiments was 20.0 cm^2. Retentate and permeate were recirculated between the feed tank and the membrane cells. Prior to filtration experiments, membranes were compacted overnight under 12.1 bar (175 psi) of pressure with DI water. Unless stated otherwise, filtration experiments were performed with an applied inlet pressure of 10.3 bar (150 psi). Pure deionized water was used when assessing the water permeance and hydraulic water permeability of the membrane. The feed solution temperature was kept constant at 25.0 ± 0.5 °C during compaction and filtration experiments. The applied inlet pressure was adjusted accordingly to compare salt rejection under the same permeate flux conditions

between the various membranes tested. Permeate and feed samples were collected after the system was allowed to equilibrate for 30 min. Feed solution pH was monitored and adjusted between 3.5 and 10.5 with sodium hydroxide (NaOH) and sulfuric acid (H_2SO_4), where the acid selected was based on feed solution. Specifically, we utilized an acid with a conjugate base dissimilar from the anion of interest to maintain a constant feed concentration during salt rejection experiments.

Water-salt permselectivity (P_W/P_S) is a material property that describes a membrane's intrinsic selectivity. This property is inextricably linked with commonly measured membrane metrics, such as the observed rejection (R_o) and water flux (J_W). We can calculate the water-salt permselectivity by accounting for concentration polarization (CP) in the diffusive boundary layer at the feed channel-membrane interface (9, 25):

$$\frac{P_W}{P_S} = \frac{R_g T}{\hat{V}_W} \frac{R_o \exp\left(\frac{J_W}{k_{sol}}\right)}{(1-R_o)\left[\Delta P - \Delta\pi \exp\left(\frac{J_W}{k_f}\right)\right]} \tag{S9}$$

where R_g, T, and $\hat{V}_W$ are the ideal gas constant (83.145 cm^3 bar K^{-1} mol^{-1}), absolute temperature (298.15 K), and specific volume of water (18 cm^3 mol^{-1}), respectively. The driving force is described by the difference between the applied hydraulic pressure (ΔP) and transmembrane osmotic pressure ($\Delta\pi_m$). The overall feed-side mass transfer coefficient (k_f), and the feed-side mass transfer coefficient for the solute of interest (k_{sol}) were estimated as 100 L m^{-2} h^{-1} so that we can utilize the measured bulk osmotic pressure difference ($\Delta\pi_b$) (9). Fig. S11 depicts the permselectivity of NF270 across various operational conditions (calculated by eq. 2). These values are based on salt rejection and water flux measurements detailed in Table S2.

Molecular Simulations of Dielectric Phenomenon

Several Lennard-Jones type water models (e.g., SPC/E (26), SPC/Fw (27), and TIP4P/ε (28), Table S3) were used to simulate water dynamics in the bulk or under confinement to ensure insensitivity to the water model. The dielectric constant of water was obtained using a box of 1,000 water molecules that was simulated with rectangular prism periodic boundary conditions and a 2 nm diameter cylinder of 1,047 water molecules for bulk and confined water, respectively (Fig. S13). The spatial confinement was enforced for the confined water model using a cylindrical harmonic wall potential with a force constant of 5,000 kcal mol^{-1} $Å^{-2}$. The cylindrical axis of the water model was not confined and was subject to a pressure of 1 atm, resulting in a minor ~5% expansion in length (up to ~112–120 Å) on average after production dynamics.

The reference-calculated dielectric constants of bulk water range from roughly 71 to 79.6, which is in good agreement with its experimental value (ε_{water} = 78.2) and validate our protocol for computing dielectric constants. The dielectric constant of water was obtained using a box of 1,000 water molecules that was simulated with rectangular prism periodic boundary conditions and a 2 nm diameter cylinder of 1,047 water molecules for bulk and confined water, respectively. The cylindrical structure was generated using Packmol (29) by randomly placing the water molecules in a cylinder of diameter 2 nm and length 10 nm with a density of 1.0 g cm^{-3}. The dimension of the unit box was then expanded to 110Å × 110Å × 110Å to avoid undesired interactions between cylinders in the radial direction. Both structures were equilibrated for 100 ps followed by 6 ns

production at a temperature of 298 K and a pressure of 1 atm in the NpT ensemble using the Nosé-Hoover thermostat and barostat (30) with temperature and pressure damping parameters of 100 and 1,000 timesteps, respectively. A time step of 1 fs for bulk water and 0.25 fs for the confined system was employed throughout in conjunction with the SHAKE algorithm (31) only for the rigid water models.

The simulation was allowed to reach steady-state conditions with 6 ns production, which is sufficient for an accurate determination of dielectric constant for various water models (32). We calculated the dielectric constant from the fluctuation in the dipole moment along the MD trajectory. Testing on bulk SPC/E water comprising 64 to 5382 water molecules all yield converging results after 4 ns production run (Fig. S13), implying dielectric constants are relatively independent of system size. Under confinement, the surface-layer dielectric constant has been reported to decrease since the rotational degree of freedom of water is hindered in proximity to the surface (33). However, in extremely confined environments such as in sub-1 nm pores, artifacts can arise in the simulations from anomalous dynamical behaviors at the potential barrier interface. Water molecules at the interface of the harmonic potential barrier feel the artificial restraining force disproportionately compared to the rest of the cylinder. The dynamics of these interfacial waters are thus influenced in a way that can lead to unrealistic perturbations in their dielectric properties. This phenomenon results in artifacts from applying such a confinement technique, seen as anomalous pronounced peaks in the center of the calculated water density profile and parallel permittivity (34, 35).

To minimize artifacts from the method, the pore size must be large enough to allow multiple water shells as buffers while still reflecting the confinement effects of inner shell water molecules. Therefore, we investigated the water shell structures for confined water cylinders with radii of 0.50 nm and 1.00 nm (Fig. S8). Specifically, we computed radial probability distribution functions $g(r)$ of water oxygen atoms with respect to the cylindrical central axis on a 4 ns trajectory subsequent to a 2 ns equilibration. Since the $g(r)$ represents the probability of finding water molecules at a certain distance from the center of the confined pore, peaks indicate where water shell structures occur. For the water cylinder with a 1.00 nm radius, the outer-shell peak ranges from 0.60 nm to 1.00 nm. Within this range, the water molecules may directly experience the artificial harmonic force but can serve to buffer the inner water shells within the 0.60 nm of the cylindrical central axis, making the boundary effects relatively insignificant. In contrast, for the water cylinder with a 0.50 nm radius pore size, the outer-shell peak ranges from 0.18 nm to 0.50 nm, which involve the majority of the water molecules in this system. In such a system, the boundary effect becomes much more severe. Therefore, we elected to model a 2-nm diameter pore to mitigate anomalous interfacial effects and emphasize only confinement effects on the dielectric constant of water molecules.

Density Functional Theory Simulations of pK_a and Molecular Binding

Here we applied density functional theory (DFT) simulations to investigate the influence of a range of dielectric environments on the pK_a of residual -COOH and -NH_2 group in the cross-linked polyamide network. The molecules 3,5-dicarbamoylbenzoic acid and acetylated-piperazine (Ace-PIP) were selected as models of R-COOH and R_2-NH_2^+, respectively, that are present in the cross-linked polyamide network. All calculations were carried out using the dispersion-corrected, range-separated hybrid functional ωB97X-D (36) with the 6-311++G(d,p) basis set. All geometry

optimizations were carried out in implicit solvent using the SMD solvation model (37). The pK_a values were calculated using a thermodynamic cycle approach, with the pK_a estimated as:

$$\mathrm{p}K_a = \frac{\Delta G}{2.303RT} = \frac{G_{HA} - G_A - G_{H^+}}{2.303RT} \quad \text{(S10)}$$

$$\mathrm{p}K_a[\text{sub, correction}] = \mathrm{p}K_a[\text{sub, DFT}] + \mathrm{p}K_a[\text{ref, EXP}] - \mathrm{p}K_a[\text{ref, DFT}] \quad \text{(S11)}$$

where entropic and zero-point energy contributions to the Gibbs free energies were obtained from an analytic Hessian calculation on the geometry optimized structure incorporating the relevant implicit solvent model. We note that "sub" and "ref" denoted in equation (S11) abbreviate substrate and reference, respectively. The proton hydration free energies were taken from previous computational benchmarks (Table S4) (38). To reduce sensitivity of computed pK_a values to both the solvent model and level of theory, we shifted all computed pK_a values by the difference of our computed pK_a values to available experimental data (39-41) across several solvents of a related compound (Tables S5-S7). For 3,5-dicarbamoylbenzoic acid, the reference compound chosen was benzoic acid, and for Ace-PIP, the reference was piperazine.

The binding enthalpy of Ace-PIP with a range of anions (i.e., ClO_4^-, ClO_3^-, NO_3^-, F^-, Cl^-, Br^-, I^-, and BO_2^-) was computed as:

$$\Delta H_{\text{binding}} = H_{\text{complex}} - H_{\text{Ace-PIP}} - H_{\text{ion}} \quad \text{(S12)}$$

where the *H* refers to the zero-point vibrational energy-corrected electronic energy (Table S8). The isolated Ace-PIP, anion, and anion-Ace-PIP complex were each geometry-optimized in implicit water solvent.

Implicit solvent models, such as the one used here (i.e., the SMD model), represent the solvent as a continuous medium with a specific dielectric constant and thus dielectric screening/response in contact with a solute of a fixed cavity size defined by the size of its substituent atoms. Such models cannot explicitly account for differences in hydrogen bonding between solvents with equivalent bulk dielectric constants. Since no explicit geometric dependence to the solvent is considered, the implicit solvent models are suited to isolate the intrinsic responses of substrate pK_a upon the variation of dielectric media. This approach provides a good approximation to understand the impact of solvents (here, water) of varying dielectric constants. Our selected basis set (6-311+G(d,p)) (38) is not at the complete basis set limit. However, since the applied correction scheme is based on experimental values, all reported calculations are expected to benefit from error cancellation that limits the effect of basis set choice.

In our study, we specifically selected five different media that span a wide range of dielectric properties, including tetrahydrofuran (THF, ε=7.6), acetone (ε=20.7), acetonitrile (ε=37.5), dimethylsulfoxide (DMSO, ε=48.0), and water (ε=78.2). In all cases, the cavity is constructed (i) via a superposition of atom-centered spheres to describe long-range electrostatics and (ii) assuming a probe radius typical of water to describe short-range solute-solvent interactions. Notably, experimental pK_a values of our reference compound benzoic acids have been measured in four of these solvent media (all except acetone). This provides a good reference for computing the pK_a of

the truncated model systems under the thermodynamic cycle scheme as we described in the method section.

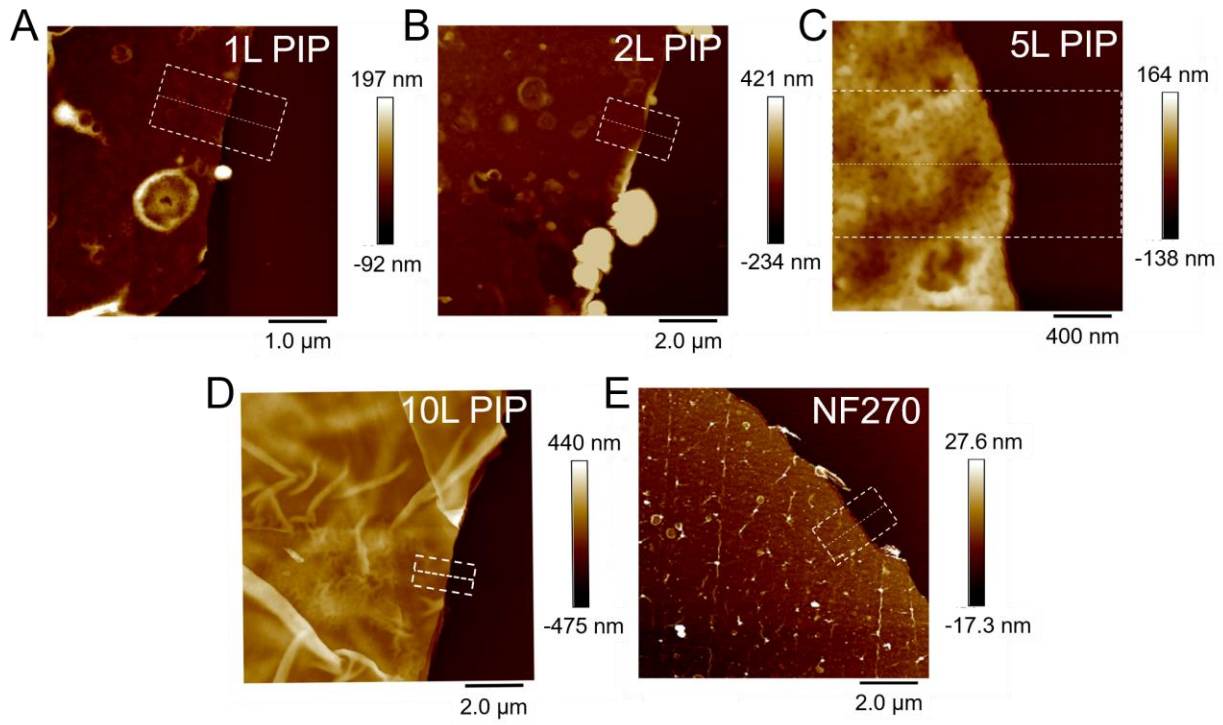

Fig. S1. Atomic force microscopy (AFM) images of polyamide films isolated on a silicon wafer. (*A*) 1L, (*B*) 2L, (*C*) 5L, and (*D*) 10L PIP films were sectioned and compared with (*E*) commercial NF270 for reference. All films were sectioned by gently scratching the film with a metal precision glide needle.

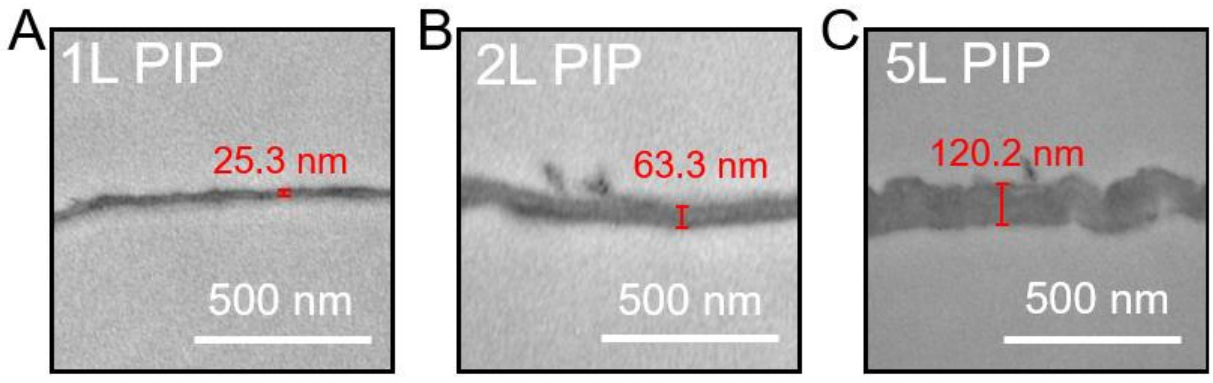

Fig. S2. Transmission electron microscopy (TEM) cross-sectional images of isolated (*A*) 1L, (*B*) 2L, and (*C*) 5L PIP films.

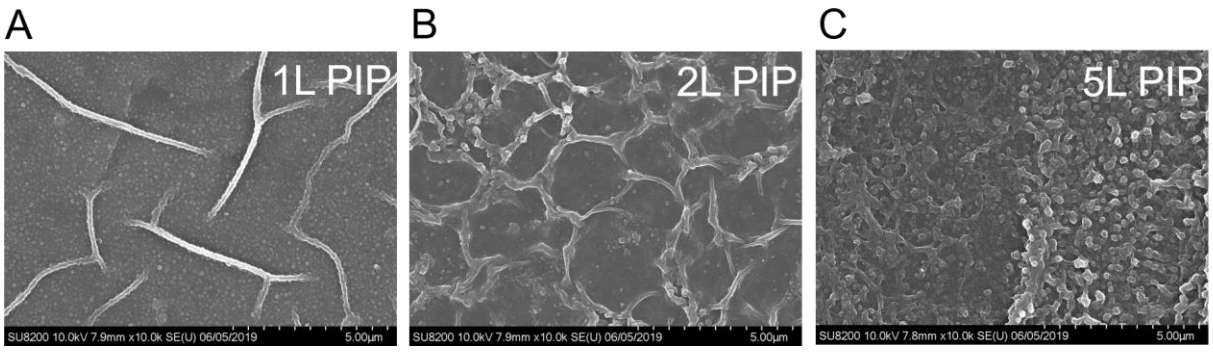

Fig. S3. Scanning electron microscopy (SEM) images of (*A*) 1L, (*B*) 2L, and (*C*) 5L PIP membrane surfaces. Membrane samples were sputter coated with 2 nm of iridium to prevent charging and increase the sample signal to noise ratio. Images were captured at 10,000× magnification.

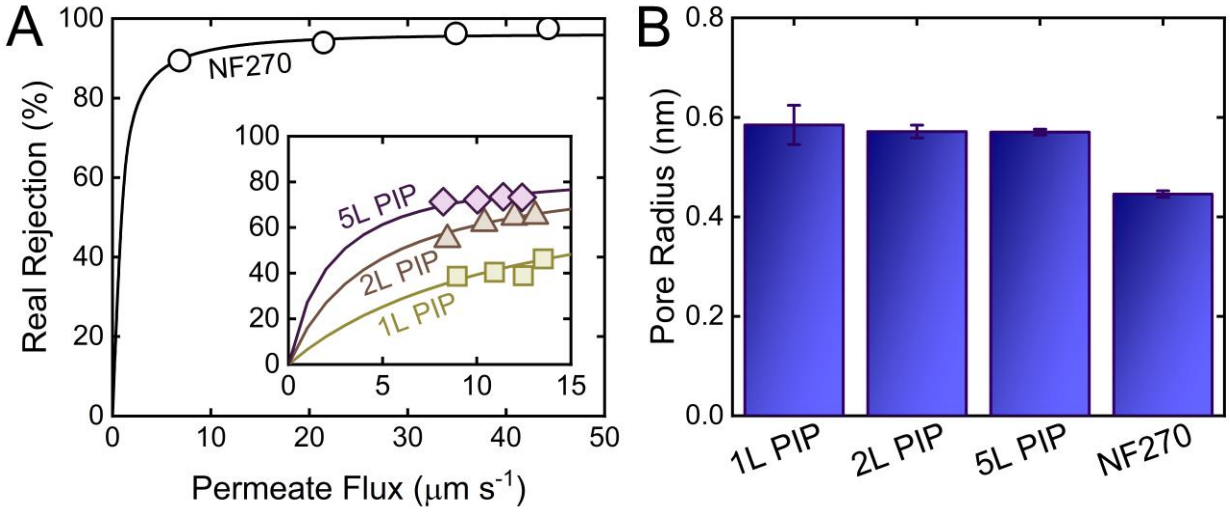

Fig. S4. Application of the hindered transport model for pore size estimation. (*A*) Real rejection of Dextrose relative to permeate flux for NF270 and LIP membranes. Solid lines represent the model fit used to estimate the (*B*) membrane pore radii. Different LIP membranes can display different rejections but still fit the same pore radius as film thickness is considered when calculating *Pe*.

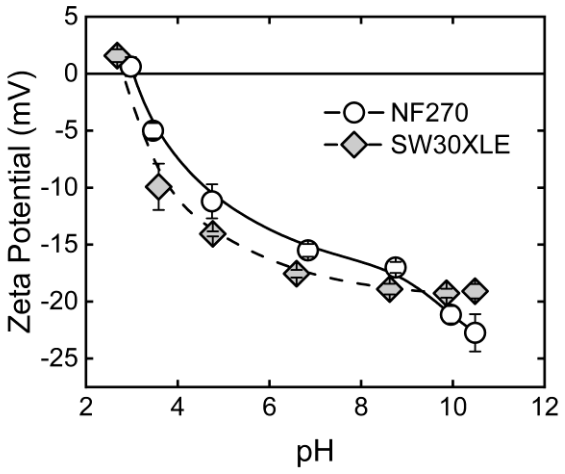

Fig. S5. Change in zeta potential with respect to pH for commercial nanofiltration (NF270) and seawater RO (SW30XLE) membranes.

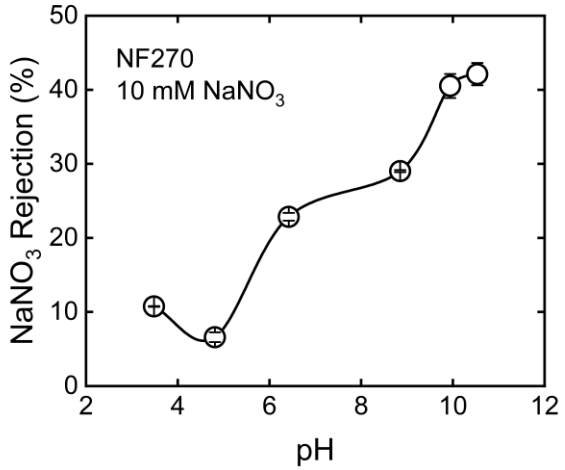

Fig. S6. Sodium nitrate ($NaNO_3$) rejection by NF270 with respect to pH, illustrating the penetration of salt into the membrane active layer.

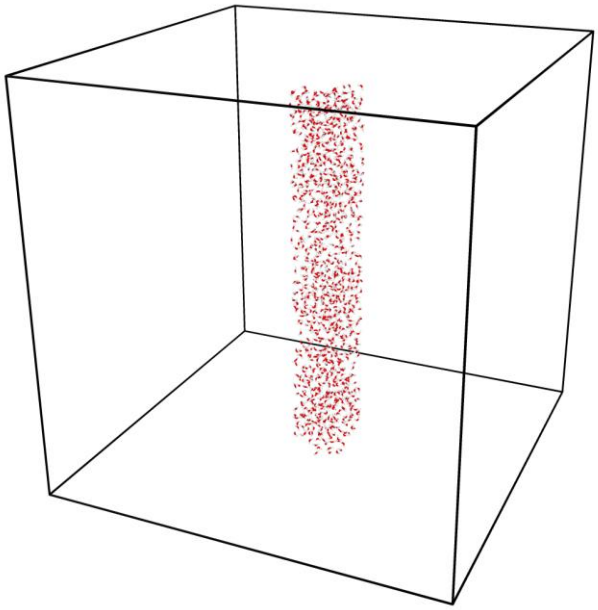

Fig. S7. Snapshot of starting configuration for molecular dynamics (MD) simulations, where water molecules are constrained by a cylindrical potential wall (ε = 1). The confined water channel is centered in the middle of a boundary unit box (black lines).

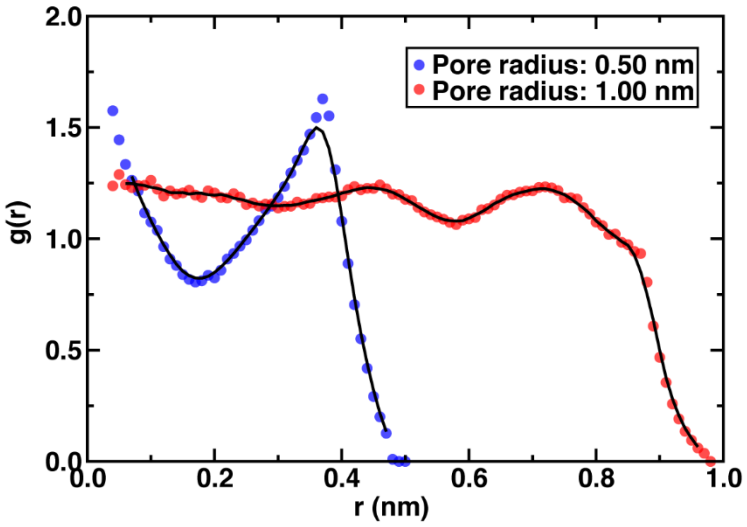

Fig. S8. Radial probability distribution function g(r) of water oxygen atoms with respect to the cylindrical central axis in the confined water cylinders. The sizes of confined water cylinders involve a radius of 0.50 nm (blue, 70% opacity) and 1.00 nm (red, 70% opacity). In both cases, g(r) is performed on 1600 frames taken from 4.0 ns of trajectories with 2.5 ps interval. The g(r) is analyzed with a starting radius of 0.05 nm and a window size of 0.01 nm. The curves in black represent running averages over a length of 0.25 nm.

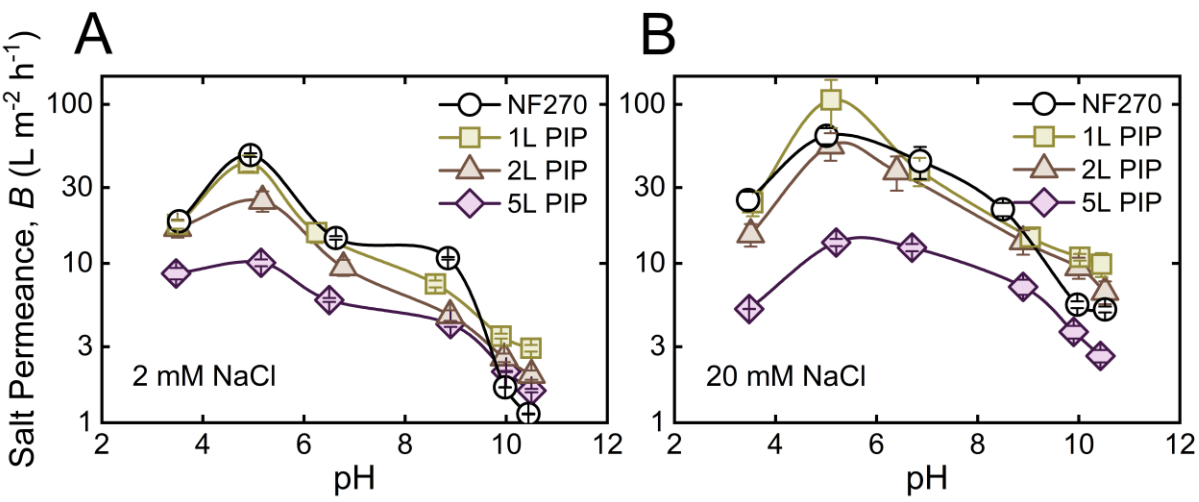

Fig. S9. Dependence of salt permeance on the number of sequential PIP layers and pH for (*A*) 2 mM and (*B*) 20 mM NaCl feed solutions. Permeance values were obtained from data presented in Fig. 5*B*-*C* of the main text, where measurements were collected under a constant water flux (J_w = 10 L m^{-2} h^{-1}) to mitigate differences in concentration polarization between membranes of varying permeability.

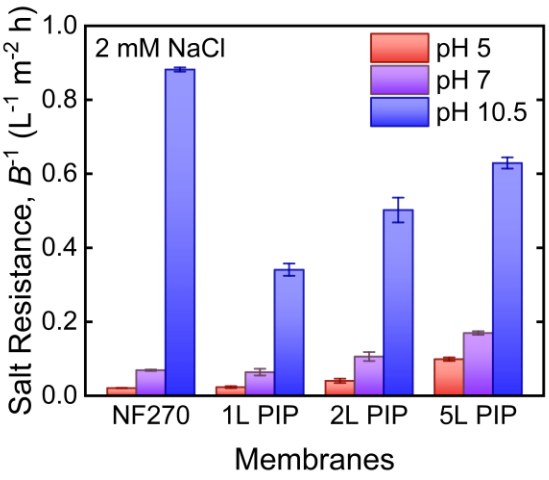

Fig. S10. Salt resistance across NF270 and LIP membranes at pH 5, 7, and 10.5. The salt resistances were taken from Fig. S9 above.

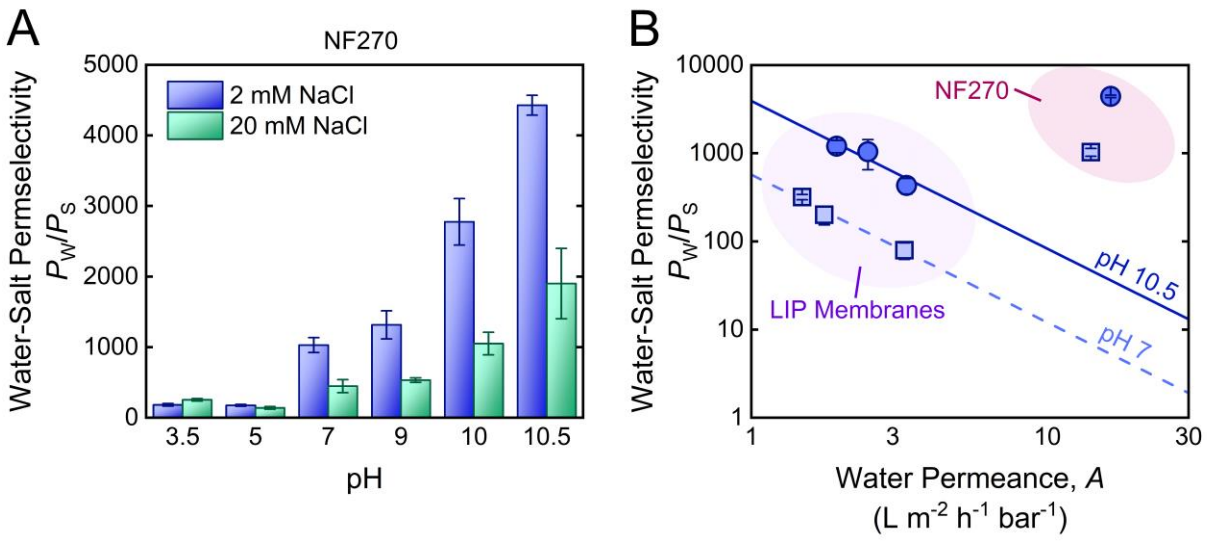

Fig. S11. Water-salt permselectivity of NF270 and LIP membranes. (*A*) Permselectivity of NF270 with respect to pH and the ionic strength of the feed solution. (*B*) Permeability-selectivity tradeoff of NF270 and LIP membranes after complete ionization of surface R-COOH (pH 7) and interior R-COOH (pH 10.5) under a feed ionic strength of 2 mM NaCl. The dashed and solid lines mark the approximate permeability-selectivity tradeoff curves for LIP membranes at pH 7 and pH 10.5, respectively. Measurements used to calculate permselectivity for NF270 are detailed in Table S2.

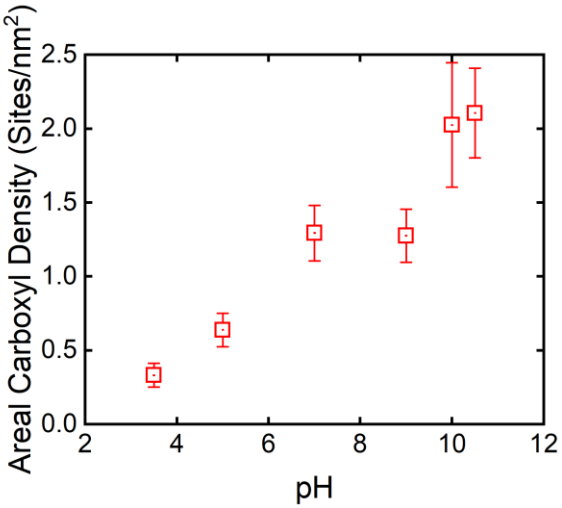

Fig. S12. Areal R-COO$^-$ density of polysulfone (PSf) support layer used during layered interfacial polymerization (LIP).

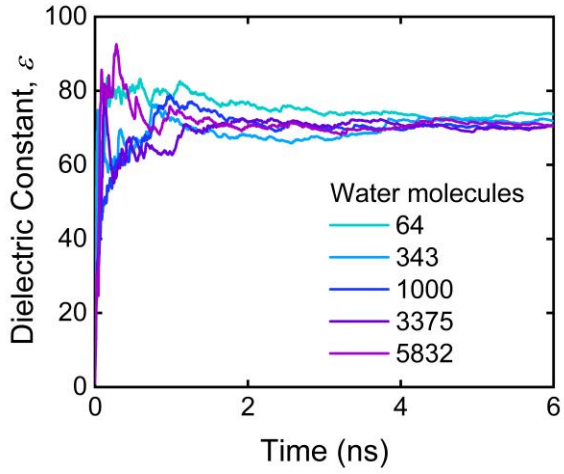

Fig. S13. Molecular dynamics simulations of the dielectric constant of bulk SPC/E water ranging from system sizes of 64 to 5832 water molecules.

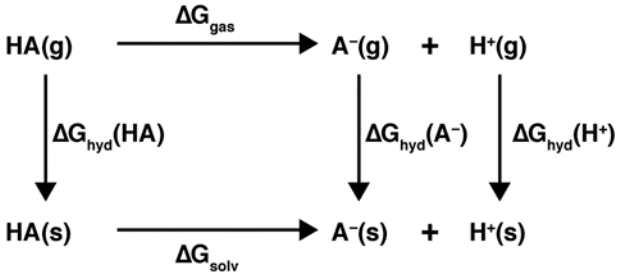

$$G(HA) = G_g(HA) + \Delta G_{hyd}(HA)$$

$$G(A^-) = G_g(A^-) + \Delta G_{hyd}(A^-)$$

$$G(H^+) = G_g(H^+) + \Delta G_{hyd}(H^+)$$

$$\Delta G_{solv} = G(HA) - G(A^-) - G(H^+)$$

$$= \Delta G_{gas} + \Delta G_{hyd}(HA) - \Delta G_{hyd}(A^-) - \Delta G_{hyd}(H^+)$$

$$pK_a = \frac{\Delta G_{solv}}{2.303RT}$$

Fig. S14 Thermodynamic cycles for pK_a calculations. G refers to free energy. HA and A^- refer to the neutral and deprotonated state of the substrate, respectively, while H^+ refers to the proton. Subscripts g and solv refer to gas phase and solvent, respectively. R is the ideal gas constant and T refers to the temperature.

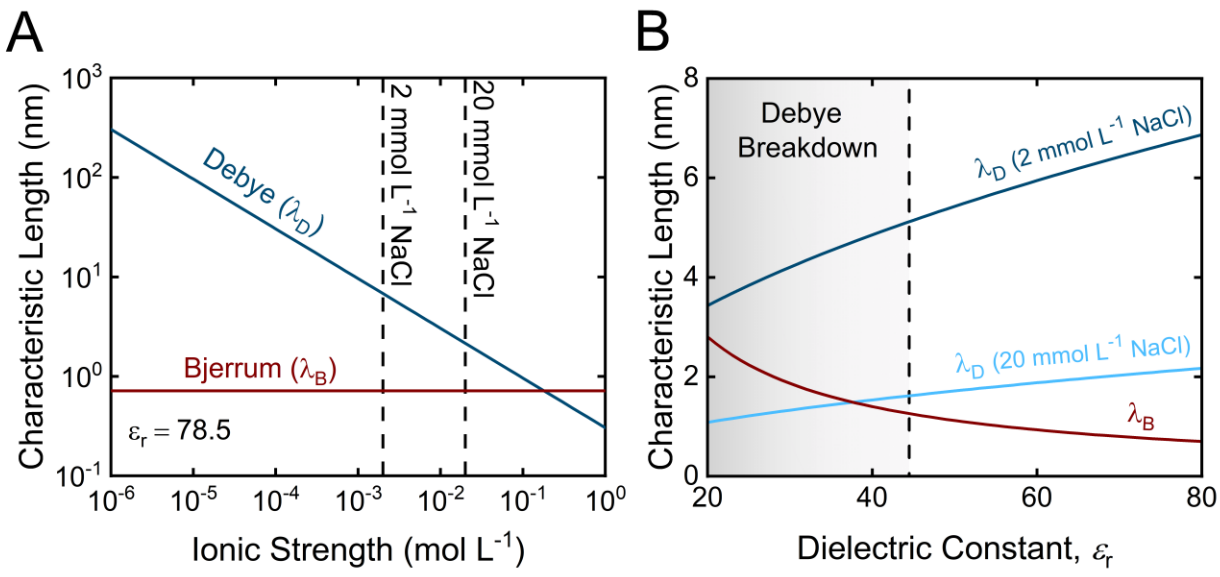

Fig. S15. Influence of solution ionic strength and dielectric constant on the characteristic Debye (λ_D) and Bjerrum (λ_B) lengths. We assumed a symmetric and monovalent electrolyte, such as NaCl, for all analyses. Characteristic length with respect to ionic strength (*A*), and dielectric constant (*B*). The dielectric constant of bulk water (ε_r = 78.5) was used when varying the ionic strength. Ionic strengths of 2 and 20 mmol L^{-1} NaCl represent the two feed solutions used in our experiments (marked with dashed lines in panel *A*). The grey shaded region in panel *B* estimates the dielectric environment in which the Debye length is inapplicable for the charged NF270 and LIP membrane pores studied here due to a breakdown in the Debye-Hückel theory.

Table S1. Relative surface areas of LIP and NF270 membranes

Membrane	Surface Area (μm^2)
NF270	1.00
1L PIP	1.10
2L PIP	1.05
5L PIP	1.19
10L PIP	1.11

Note: surface areas were measured over a 1 μm^2 projected area by atomic force microscopy

Table S2. Measured values for calculating NF270 permselectivity

Feed Solution	pH	Observed Rejection, R_o (%)	Water Flux, J_W (L m^{-2} h^{-1})
2 mM NaCl	3.5	23.66 ± 0.88	147.8 ± 5.1
	5	21.83 ± 1.15	154.8 ± 3.9
	7	67.08 ± 1.03	132.4 ± 5.8
	9	74.82 ± 1.93	118.5 ± 5.2
	10	85.31 ± 1.08	126.5 ± 3.2
	10.5	87.60 ± 1.49	153.6 ± 11.5
20 mM NaCl	3.5	28.63 ± 1.30	151.5 ± 4.1
	5	18.25 ± 1.44	150.2 ± 3.3
	7	45.01 ± 4.32	135.7 ± 4.3
	9	55.58 ± 0.64	113.0 ± 3.8
	10	68.33 ± 1.16	125.1 ± 8.9
	10.5	71.26 ± 4.17	165.7 ± 3.6

Note: measurements were taken in triplicate under an applied hydraulic pressure of 150 psi.

Table S3. Parameters and calculated dielectric constant of water models

Water Model	q_H (e)	q_O (e)	σ_{OO} (Å)	ε_{OO} (kcal mol^{-1})	Dielectric constant
SPC/E (29)	+0.4238	-0.8476	3.166	0.1554	71.0
SPC/Fw (30)	+0.4100	- 0.8200	3.166	0.1554	79.6
TIP4P/ε (31)	+0.5270	- 1.0540	3.165	0.1848	78.3

Table S4. Proton hydration free energies in different solvents

Solvent	THF	Acetone	Acetonitrile	DMSO	Water
G_{H+} (kJ mol^{-1})	-1047.6	-1066.9	-1054.5	-1120.7	-1062.9

Note: values are based on previous computational benchmarks (28).

Table S5. Free energies, pK_a, and correction factors for Benzoic Acid

Solvent	G_{HA} (Hartree)	G_{A-} (Hartree)	G_{H+} (Hartree)	ΔG (kcal mol^{-1})	pK_a	Expl. pK_a	Correction factor
THF	-420.7270	-420.2506	-0.3990	48.6	35.2	25.1	10.1
Acetone	-420.7285	-420.2639	-0.4016	39.5	28.6	-	6.2[a]
Acetonitrile	-420.7283	-420.2662	-0.4016	37.9	27.5	21.3	6.2

Note: The energies were optimized using ωB97X-D (32) with the 6-311++G(d,p) basis set. The solvent model is SMD (33). [a]Due to the lack of experimental pK_a for benzoic acid in acetone, the correction factor was taken based on the results from acetonitrile.

Table S6. Free energies, pK_a, and correction factors for 3,5-dicarbamoylbenzoic acid

Solvent	G_{HA} (Hartree)	G_{A-} (Hartree)	G_{H+} (Hartree)	ΔG (kcal mol^{-1})	pK_a	Expl. pK_a	Correction factor
THF	-758.1059	-757.6402	-0.3990	41.9	30.3	10.1	20.2
Acetone	-758.1106	-757.6512	-0.4016	36.2	26.2	6.2	20.0
Acetonitrile	-758.1101	-757.6528	-0.4016	35.0	25.3	6.2	19.1
DMSO	-758.1094	-757.6511	-0.4268	19.8	14.3	5.4	8.9
Water	-758.1130	-757.6701	-0.4048	23.9	17.3	14.4	2.9

Note: The energies were optimized using ωB97X-D (32) with the 6-311++G(d,p) basis set. The solvent model is SMD (33).

Table S7. Free energies, pK_a, and correction factors for acetylated-piperazine

Solvent	G_{HA} (Hartree)	G_{A-} (Hartree)	G_{H+} (Hartree)	ΔG (kcal mol^{-1})	pK_a	Expl. pK_a	Correction factor
THF	-420.8946	-420.4504	-0.3990	28.4	20.5	10.1	10.5
Acetone	-420.9072	-420.4532	-0.4016	32.8	23.8	6.2	17.6
Acetonitrile	-420.9094	-420.4531	-0.4016	34.3	24.8	6.2	18.6
DMSO	-420.9081	-420.4510	-0.4268	19.0	13.8	5.4	8.4
Water	-420.9069	-420.4555	-0.4048	29.2	21.1	14.4	6.7

Note: The energies were optimized using ωB97X-D (32) with the 6-311++G(d,p) basis set. The solvent model is SMD (33).

Table S8. Enthalpies of acetylated-piperazine (Ace-PIP) binding to anions

Anion	$H_{complex}$ (Hartree)	H_{ion} (Hartree)	$H_{Ace\text{-}PIP}$ (Hartree)	$\Delta H_{binding}$ (kcal mol^{-1})
F^-	-520.8856	-99.9939	-420.8645	-17.0
Cl^-	-881.2623	-460.3844	-420.8645	-8.4
Br^-	-434.2259	-13.3274	-420.8645	-21.3
I^-	-432.4559	-11.5803	-420.8645	-7.0
ClO_3^-[a]	-1106.6314	-685.7595	-420.8627	-5.8
ClO_4^-[a]	-1181.7589	-760.8897	-420.8627	-4.1
NO_3^-[a]	-701.3135	-280.4404	-420.8627	-6.5

Note: the energies were optimized using ωB97X-D (32) with the 6-311++G(d,p) basis set. The solvent model is SMD (33). [a]Due to failure of convergence in geometric optimization, we instead optimize the geometries using ωB97X-D (32) with the 6-31G(d) basis set and then compute the single point energies using the 6-311++G(d,p) basis set.

Supplementary References

1. L. D. Nghiem, A. I. Schafer, M. Elimelech, Removal of natural hormones by nanofiltration membranes: Measurement, modeling, and mechanisms. *Environ. Sci. Technol.* **38**, 1888-1896 (2004).
2. E. Drazevic, K. Kosutic, V. Kolev, V. Freger, Does hindered transport theory apply to desalination membranes? *Environ. Sci. Technol.* **48**, 11471-11478 (2014).
3. M. Xie, L. D. Nghiem, W. E. Price, M. Elimelech, Relating rejection of trace organic contaminants to membrane properties in forward osmosis: Measurements, modelling and implications. *Water Res.* **49**, 265-274 (2014).
4. W. M. Deen, Hindered transport of large molecules in liquid-filled pores. *AIChE J.* **33**, 1409-1425 (1987).
5. A. E. Childress, M. Elimelech, Effect of solution chemistry on the surface charge of polymeric reverse osmosis and nanofiltration membranes. *J. Membr. Sci.* **119**, 253-268 (1996).
6. A. E. Childress, M. Elimelech, Relating nanofiltration membrane performance to membrane charge (electrokinetic) characteristics. *Environ. Sci. Technol.* **34**, 3710-3716 (2000).
7. M. Bauman, A. Kosak, A. Lobnik, I. Petrinic, T. Luxbacher, Nanofiltration membranes modified with alkoxysilanes: Surface characterization using zeta-potential. *Colloids Surf. Physicochem. Eng. Asp.* **422**, 110-117 (2013).
8. J. Q. Luo, Y. H. Wan, Effects of pH and salt on nanofiltration—a critical review. *J. Membr. Sci.* **438**, 18-28 (2013).
9. J. R. Werber, A. Deshmukh, M. Elimelech, The critical need for increased selectivity, not increased water permeability, for desalination membranes. *Environ. Sci. Tech. Let.* **3**, 112-120 (2016).
10. C. Boo *et al.*, High performance nanofiltration membrane for effective removal of perfluoroalkyl substances at high water recovery. *Environ. Sci. Technol.* **52**, 7279-7288 (2018).
11. D. Chen, J. R. Werber, X. Zhao, M. Elimelech, A facile method to quantify the carboxyl group areal density in the active layer of polyamide thin-film composite membranes. *J. Membr. Sci.* **534**, 100-108 (2017).
12. V. Freger, Ion partitioning and permeation in charged low-T* membranes. *Adv. Colloid Interface Sci.* **277**, 102107 (2020).
13. S. Bason, V. Freger, Phenomenological analysis of transport of mono- and divalent ions in nanofiltration. *J. Membr. Sci.* **360**, 389-396 (2010).
14. N. Kavokine, S. Marbach, A. Siria, L. Bocquet, Ionic coulomb blockade as a fractional wien effect. *Nat. Nanotechnol.* **14**, 573-578 (2019).
15. W. H. Guan, S. X. Li, M. A. Reed, Voltage gated ion and molecule transport in engineered nanochannels: Theory, fabrication and applications. *Nanotechnology* **25**, 122001 (2014).

16. J. Kamcev, D. R. Paul, B. D. Freeman, Ion activity coefficients in ion exchange polymers: Applicability of manning's counterion condensation theory. *Macromolecules* **48**, 8011-8024 (2015).

17. J. M. S. Henis, M. K. Tripodi, Composite hollow fiber membranes for gas separation – the resistance model approach. *J. Membr. Sci.* **8**, 233-246 (1981).

18. M. Cheryan, *Ultrafiltration and Microfiltration Handbook* (Technomic Publishing Co., Inc., Lancaster, UK, 1998).

19. R. Epsztein, E. Shaulsky, N. Dizge, D. M. Warsinger, M. Elimelech, Role of ionic charge density in donnan exclusion of monovalent anions by nanofiltration. *Environ. Sci. Technol.* **52**, 4108-4116 (2018).

20. F. A. Pacheco, I. Pinnau, M. Reinhard, J. O. Leckie, Characterization of isolated polyamide thin films of RO and NF membranes using novel TEM techniques. *J. Membr. Sci.* **358**, 51-59 (2010).

21. O. Coronell, B. J. Marinas, D. G. Cahill, Accessibility and ion exchange stoichiometry of ionized carboxylic groups in the active layer of FT30 reverse osmosis membrane. *Environ. Sci. Technol.* **43**, 5042-5048 (2009).

22. O. Coronell, M. I. Gonzalez, B. J. Marinas, D. G. Cahill, Ionization behavior, stoichiometry of association, and accessibility of functional groups in the active layers of reverse osmosis and nanofiltration membranes. *Environ. Sci. Technol.* **44**, 6808-6814 (2010).

23. O. Coronell, B. J. Marinas, D. G. Cahill, Depth heterogeneity of fully aromatic polyamide active layers in reverse osmosis and nanofiltration membranes. *Environ. Sci. Technol.* **45**, 4513-4520 (2011).

24. D. F. Sunday, E. P. Chan, S. V. Orski, R. C. Nieuwendaal, C. M. Stafford, Functional group quantification of polymer nanomembranes with soft x-rays. *Phys. Rev. Mater.* **2**, 032601 (2018).

25. G. M. Geise, D. R. Paul, B. D. Freeman, Fundamental water and salt transport properties of polymeric materials. *Prog. Polym. Sci.* **39**, 1-42 (2014).

26. H. J. C. Berendsen, J. R. Grigera, T. P. Straatsma, The missing term in effective pair potentials. *J. Phys. Chem.* **91**, 6269-6271 (1987).

27. R. Fuentes-Azcatl, M. C. Barbosa, Thermodynamic and dynamic anomalous behavior in the TIP4P/ε water model. *Physica A* **444**, 86-94 (2016).

28. Y. J. Wu, H. L. Tepper, G. A. Voth, Flexible simple point-charge water model with improved liquid-state properties. *J. Chem. Phys.* **124**, 024503 (2006).

29. L. Martinez, R. Andrade, E. G. Birgin, J. M. Martinez, Packmol: A package for building initial configurations for molecular dynamics simulations. *J. Comput. Chem.* **30**, 2157-2164 (2009).

30. M. E. Tuckerman, Y. Liu, G. Ciccotti, G. J. Martyna, Non-hamiltonian molecular dynamics: Generalizing hamiltonian phase space principles to non-hamiltonian systems. *J. Chem. Phys.* **115**, 1678-1702 (2001).

31. J. P. Ryckaert, G. Ciccotti, H. J. C. Berendsen, Numerical-integration of cartesian equations of motion of a system with constraints – molecular-dynamics of n-alkanes. *J. Comput. Phys.* **23**, 327-341 (1977).

32. O. Gereben, L. Pusztai, On the accurate calculation of the dielectric constant from molecular dynamics simulations: The case of SPC/E and SWM4-DP water. *Chem. Phys. Lett.* **507**, 80-83 (2011).

33. L. Fumagalli *et al.*, Anomalously low dielectric constant of confined water. *Science* **360**, 1339-1342 (2018).

34. M. H. Motevaselian, S. Y. Mashayak, N. R. Aluru, Extended coarse-grained dipole model for polar liquids: Application to bulk and confined water. *Phys. Rev. E* **98**, 052135 (2018).

35. C. Schaaf, S. Gekle, Spatially resolved dielectric constant of confined water and its connection to the non-local nature of bulk water. *J. Chem. Phys.* **145**, 084901 (2016).

36. J. D. Chai, M. Head-Gordon, Long-range corrected hybrid density functionals with damped atom-atom dispersion corrections. *Phys. Chem. Chem. Phys.* **10**, 6615-6620 (2008).

37. A. V. Marenich, C. J. Cramer, D. G. Truhlar, Universal solvation model based on solute electron density and on a continuum model of the solvent defined by the bulk dielectric constant and atomic surface tensions. *J. Phys. Chem. B* **113**, 6378-6396 (2009).

38. I. A. Topol, G. J. Tawa, S. K. Burt, A. A. Rashin, Calculation of absolute and relative acidities of substituted imidazoles in aqueous solvent. *J. Phys. Chem. A* **101**, 10075-10081 (1997).

39. A. Kütt *et al.*, p*K*(a) values in organic chemistry – making maximum use of the available data. *Tetrahedron Lett.* **59**, 3738-3748 (2018).

40. F. Khalili, A. Henni, A. L. L. East, p*K*(a) values of some piperazines at (298, 303, 313, and 323) K. *J. Chem. Eng. Data* **54**, 2914-2917 (2009).

41. D. D. Perrin, *Dissociation Constants of Organic Bases in Aqueous Solution* (Butterworths, London, 1972).